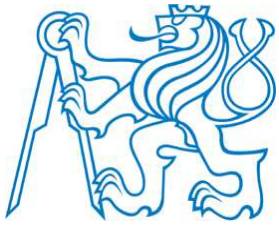

CZECH TECHNICAL UNIVERSITY IN PRAGUE

Faculty of Electrical Engineering
Department of Electromagnetic Field

Detection of high refractive index liquids by plastic optical fibers with enhanced evanescent wave

Master's Thesis

Study program: Communications, Multimedia and Electronics
Branch of study: Wireless Communications

Master student: Bc. Anastasiya Rakitina
Supervisor: Ing. Matěj Komanec, Ph.D.
Co-superviser: Ing. Tomáš Němeček

Prague, 2017

ČESKÉ VYSOKÉ UČENÍ TECHNICKÉ V PRAZE

ZADÁNÍ DIPLOMOVÉ PRÁCE

I. OSOBNÍ A STUDIJNÍ ÚDAJE

Příjmení: **Rakitina** Jméno: **Anastasiya** Osobní číslo: **392832**

Fakulta/ústav: **Fakulta elektrotechnická**

Zadávající katedra/ústav: **Katedra elektromagnetického pole**

Studijní program: **Komunikace, multimédia a elektronika**

Studijní obor: **Bezdrátové komunikace**

II. ÚDAJE K DIPLOMOVÉ PRÁCI

Název diplomové práce:

Detection of High Refractive Index Liquids by Plastic Optical Fibers with Enhanced Evanescent Wave

Název diplomové práce anglicky:

Detection of High Refractive Index Liquids by Plastic Optical Fibers with Enhanced Evanescent Wave

Pokyny pro vypracování:

The aim of the diploma thesis will be at first a theoretical analysis of the detection of liquids using optical fibers with the emphasis on liquids with refractive indices higher than the refractive index of fused silica. The student will focus on optical sensing based on the refractometric principle utilizing enhanced evanescent wave. In a simulation environment, tapered and D-shaped fiber structures will be analyzed for a selected set of liquids in the refractive index range over 1.45 with regard to the mode-field distribution and wavelength. The main part of the thesis will be focused on an experimental campaign, where detection of specific liquid analytes will be carried out utilizing shape-tailored plastic optical fibers. The diploma thesis will finally include a comparison of theoretical and experimental results.

Seznam doporučené literatury:

[1] Novotný K., Martan T., Šístek J.: Systémy pro optické komunikace. Vydavatelství ČVUT. Praha 2007
[2] De-Jun F., Guan-Xiu L., Xi-Lu L., Ming-Shun J., and Qing-Mei S., 'Refractive index sensor based on plastic optical fiber with tapered structure,' Appl. Opt. 53, 2007-2011 (2014)

Jméno a pracoviště vedoucí(ho) diplomové práce:

Ing. Matěj Komanec Ph.D., katedra elektromagnetického pole FEL

Jméno a pracoviště druhé(ho) vedoucí(ho) nebo konzultanta(ky) diplomové práce:

Datum zadání diplomové práce: **16.02.2017** Termín odevzdání diplomové práce: _____

Platnost zadání diplomové práce: **25.05.2018**

Podpis vedoucí(ho) práce	Podpis vedoucí(ho) ústavu/katedry	Podpis děkana(ky)

III. PŘEVZETÍ ZADÁNÍ

Diplomantka bere na vědomí, že je povinna vypracovat diplomovou práci samostatně, bez cizí pomoci, s výjimkou poskytnutých konzultací. Seznam použité literatury, jiných pramenů a jmen konzultantů je třeba uvést v diplomové práci.

Datum převzetí zadání	Podpis studentky

Abstrakt

Předkládaná práce se zabývá problematikou detekce kapalin o indexu lomu vyšším než 1,45. Je teoreticko-praktického charakteru se zaměřením na optickou detekci založenou na principu refraktometrie se zvýšenou evanescentní vlnou.

Nejdříve jsou shrnuty teoretické podklady. Poté jsou realizovány senzorické struktury vláken pro detekci kapalin v simulačním prostředí. Je navrženo schéma zapojení pro měření indexu lomu pomocí tvarovaných optických vláken.

Praktická část práce je věnována provedení měření s navrženou senzorickou strukturou na bázi plastového optického vlákna a vyhodnocení dosažených výsledků.

Klíčová slova: optické vlákno, index lomu, evanescentní vlna, refraktometrie, detekce kapalin, senzor, citlivost.

Abstract

This thesis deals with detection of liquids with refractive index higher than 1,45. The project covers both, theoretical and practical aspects of the question with focus on optical sensing based on the refractometric principle utilizing enhanced evanescent wave.

First, some theoretical aspects are presented. Then, optical fiber sensor structures for detection of liquids are implemented by using a simulation environment. A measurement setup is proposed for carrying out the experimental campaign utilizing shape-tailored optical fibers.

The practical part presents the measurements with the proposed sensor structure based on plastic optical fiber and evaluates the obtained results.

Key words: optical fiber, refractive index, evanescent wave, refractometry, detection of liquids, sensor, sensitivity.

Acknowledgement

I would like to thank my supervisor Ing. Matěj Komanec, Ph.D. for his patience and guidance, for the time Ing. Matěj Komanec, Ph.D. devoted to checking this thesis and his helpful comments.

I am also thankful to Ing. Tomáš Němeček for his help with providing the measurements and his useful advice.

Declaration

I declare that I worked out this thesis by myself and I cited all the used sources of information in accordance with the Methodological Instructions on Observation of Ethical Principles during the Preparation of University Final Theses issued by the Czech Technical University in Prague.

Prague, May 26, 2017 …….

Content

List of Figures

List of Tables

List of Abbreviations

FOS – fiber-optic sensor

EMI – electromagnetic interference

RI – refractive index

TIR – total internal reflection

OSA – optical spectrum analyzer

POF – plastic optical fiber

PMMA – polymethylmethacrylate

NA – numerical aperture

IPA – isopropyl alcohol

RIU – refractive index unit

Introduction

Fiber-optic sensors (FOS) are devices based on an optical fiber as a sensing element. They are used to detect physical quantities like temperature, pressure or, for example, mechanical strain as well as vibrations, rotation, concentrations of chemical species etc. The idea of FOS is that light from a source is sent through an optical fiber, where it experiences changes of its parameters, and then reaches a detector which quantifies these changes.

FOS have some attractive advantages over other types of sensors. It makes them unique for certain types of applications. The main advantages of FOS are:

- FOS are small and lightweight, which makes it possible to use them for both embedding and surface mounting;
- FOS consist of electrically insulating materials, so they can be safely used in high-voltage and explosive environments (there is no risk of electrical sparks);
- FOS are resistant to electromagnetic interference (EMI) and do not themselves affect other devices;
- FOS can operate in a wide range of temperatures and handle extreme conditions;
- FOS are biocompatible and non-intrusive, so can be used for medical applications or in food industry. [1]

Due to this, FOS have gained popularity in numerous applications in industries, one of which is liquid refractive index sensing. It is widespred, for example, in food production or in chemical and biomedical applications for detection of mineral (or paraffin) oils. Since these types of oils have refractive indices (RI) in the range from ~1,45, which is higher than the refractive index of silica, it is necessary to use an alternative to silica glass optical fiber (for example, a plastic optical fiber).

1. Theoretical background

1.1. Optical fiber modes

While being guided through the fiber, the light waves exhibit so-called modes, which are variations in the intensity of the light (both, over the fiber cross-section and along the length of the fiber). These modes represent certain patterns of the waves formed within the fiber, as, in a very simple sense, they determine the way the light waves propagate through the fiber. This set of electromagnetic fields propagating in the optical fiber is called guided (or propagation) modes. They are defined by the optical fiber geometry and its material composition (the variation of the refractive indices of the fiber core and cladding across the cross-section). Guided modes are confined to the core. They carry energy along the fiber, transporting, therefore, power and information. [1, 2]

Light rays which are launched into the fiber with an angle higher than the fiber acceptance angle are not guided by the core region, but make radiation (or unbound) modes. They carry energy out of the core. Partially, this radiation is trapped in the cladding and formes so-called cladding modes. Since the core and the cladding modes propagate along the fiber, mode coupling can occur between them. It results in a power transfer back and forth between these two types of modes, resulting into the core modes power loss.

In addition to the bound and radiation modes, a third category called tunneling (or leaky) modes is also present in optical fibers. These modes are only partially confined to the core region, and are attenuated by continuously radiating their power out of the core as they propagate along the fiber. [3]

Light rays can propagate within the optical fiber in two distinct types: meridional rays and skew ones.

Meridional rays (see Figure 1.1) travel in the meridional planes of the fiber. These planes contain the axis of symmetry of the fiber (the core axis).

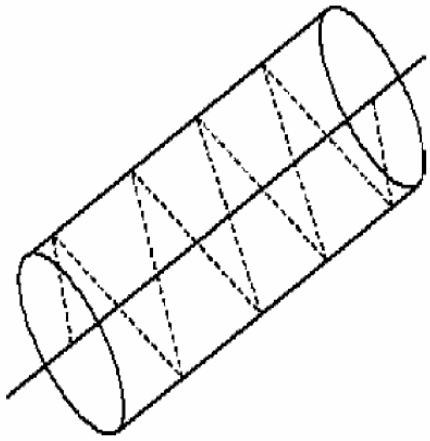

Figure 1.1 – Illustration of a meridional ray propagating in an optical fiber core [3].

Unlike meridional rays, which lie in a single plane, skew rays (see Figure 1.2) follow a helical (non-planar zig-zag) path along the fiber and do not cross the fiber axis.

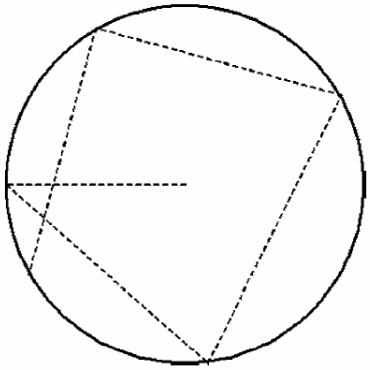

Figure 1.2 – Illustration of a skew ray propagating in an optical fiber core (transverse cross-sectional view) [3].

1.2. Evanescent wave of an optical fiber

It appears that in the situation of total internal reflection (TIR) at the core-cladding interface within the fiber, when the angle of incidence exceeds the critical angle, there is no a transmitted wave and the light rays (and so the energy) are totally reflected. However, the light gets through the boundary and extends into the second (refractive) medium as so-called evanescent wave. The evanescent wave amplitude decreases exponentially with distance away from the interface (see Figure 1.3). [4, 5]

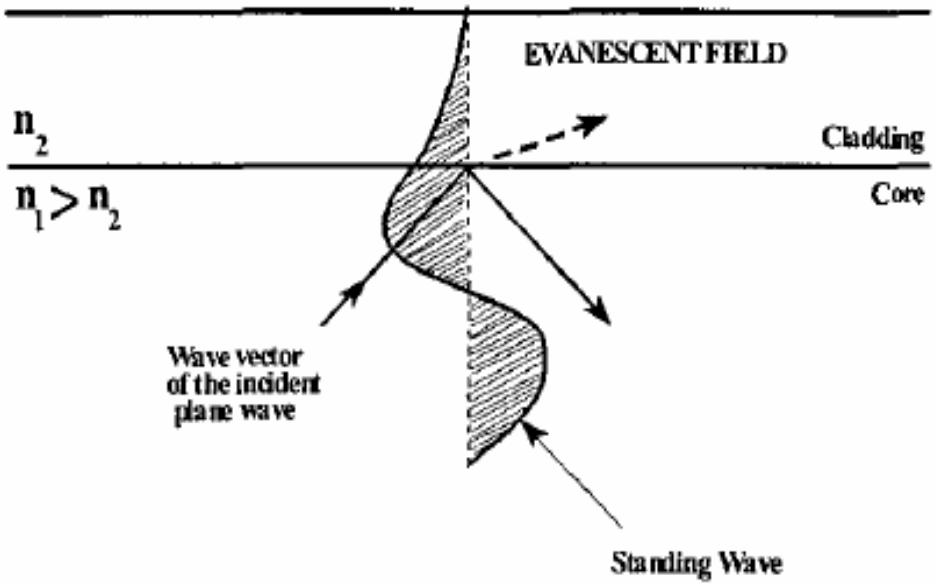

Figure 1.3 – Evanescent wave illustration [2].

The degree of evanescent wave penetration into the refractive medium is called the penetration depth, d_p. It is defined as the distance from the core-cladding boundary at which the evanescent wave amplitude is 1/*e* of its value at the boundary:

$$d_p = \frac{\lambda}{2\pi\sqrt{n_{co}^2 \sin^2\theta - n_{cl}^2}} \tag{1.1}$$

where λ is the wavelength of the light source, θ is the angle of incidence at the core-cladding boundary and n_{co} and n_{cl} are the refractive indices of the core and cladding respectively. [6]

1.3. Optical fiber refractometry

Refractometry is a technique for measuring substances' RI in order to, for example, identify an unknown liquid compound (our case) or its purity by comparing the measured RI to known literature values.

The RI is a unitless number. It is dependent on temperature and the wavelength used. Therefore, it must be taken into account in case of differences from reference values, which usually are 20 °C (reference temperature) and 589,3 nm (reference wavelength, indicates the sodium D line).

The RI is typically reported as:

$$n_D^{20} \tag{1.2}$$

where *n* represents the refractive index, the superscript indicates the temperature in degrees Celsius, and the subscript denotes the wavelength. [7]

There are many methods for measuring RI with optical fiber sensors. One of them is based on direct interaction of the substance under test with the evanescent wave of the fiber. To insure the interaction, which is proportional to the penetration depth, it is necessary to have the closest possible approach to the core of the fiber.

The simpliest way how to achieve this is to remove the protective coating of the fiber and reduce the cladding, which in itself is non-absorbing and so light propagates along the fiber with almost no energy loss due to it. Thus, the absorbing substance replaces the cladding and interacts with the evanescent field of the fiber. Its intensity is, therefore, attenuated and the total transmitted energy in the fiber is reduced. [8]

The interaction with the evanescent field is proportional to its penetration depth. It is, in turn, related to the opto-geometrical parameters of a fiber, which are generalized in the fiber's normalized frequency *V*:

$$V = \frac{2\pi r}{\lambda}\sqrt{n_{co}^2 - n_{ext}^2} \tag{1.3}$$

where λ is the light wavelength, r is the fiber core radius, n_{co} is the refractive index of the fiber core and n_{ext} is the refractive index of the external environment (which replaces the cladding). [4]

As it can be seen from Equation (1.3), the fiber's normalized frequency is dependent on the parameter n_{ext}. Thus, the refractive index can be monitored by measuring the transmission loss change resulted from the normalized frequency variation. [9]

But in this simple configuration, when the cladding is just removed uniformly over a segment of the fiber and replaced by analyte, the evanescent field penetration depth is not typically sufficient enough for efficient sensing.

To overcome this problem, so as to increase the interaction with the evanescent field, different methods have been put forward, such as fiber bending, use of special fibers (for example, D-fibers or microstructured fibers), fiber tapering etc. [6]

1.4. Tapered fiber

1.4.1. Tapered fiber structure

A tapered fiber is a structure, where an optical fiber diameter is reduced over a defined length (see Figure 1.4). The smallest diameter segment of this structure is called a taper waist. Between the uniform untapered parts and the waist there are so-called transition regions. The waist diameter can vary from a few micrometers to several tens of micrometers (depending on the tapered fiber application). Similarly, the taper waist length can change from a few millimeters to several tens of centimeters.

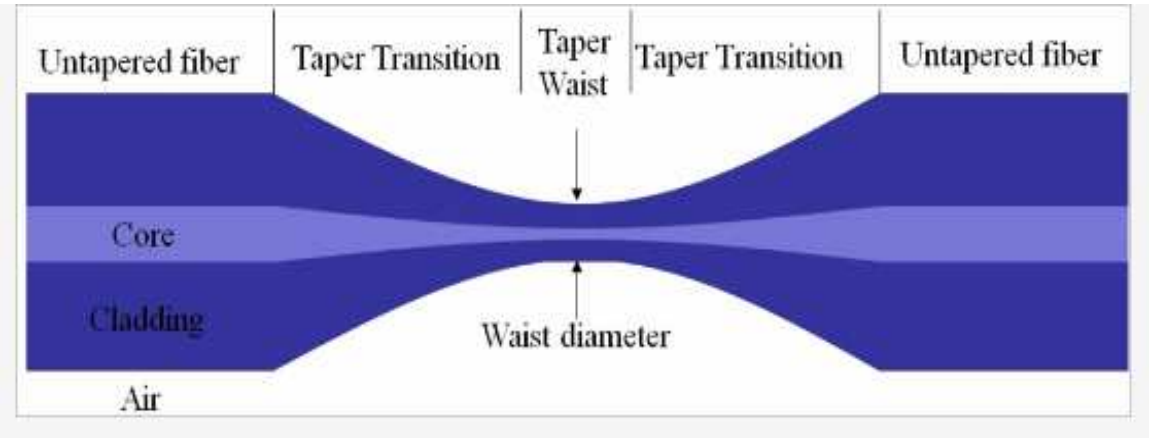

Figure 1.4 – Schematic of a tapered fiber [10].

In the tapered part the normalized frequency V_{taper} is:

$$V_{taper} = \frac{2\pi r_{tot}(z)}{\lambda}\sqrt{n_{co}^2 - n_{ext}^2} \tag{1.4}$$

where z is the coordinate along the optical fiber and r_{tot} is the radius of the tapered fiber as a function of z. [9]

According to the Equation (1.4), the diameter and the tapered segment length both influence the normalized frequency of a tapered fiber. Consequently, the transmitted power depends on the variation of the tapered region's parameters. For example, for low loss tapered fibers the adiabaticity criterion must be observed: the relative local change of the taper diameter must be very small (the taper is gradual). On the other hand, different shape considerations take place if tapered fibers are used as sensors.

Nowadays, there are a number of configurations of sensors based on tapered optical fibers. They are, for example, straight biconical tapers, tapered fiber tips, periodically tapered structures, tapers with functionalized surfaces etc., each of which best suits certain applications. [6]

1.4.2. Tapered fiber fabrication

The most widespread way to manufacture a taper is to utilize the flame-heating technique to stretch and taper an optical fiber. Figure 1.5 shows a schematic illustration of tapered fiber fabrication based on this method.

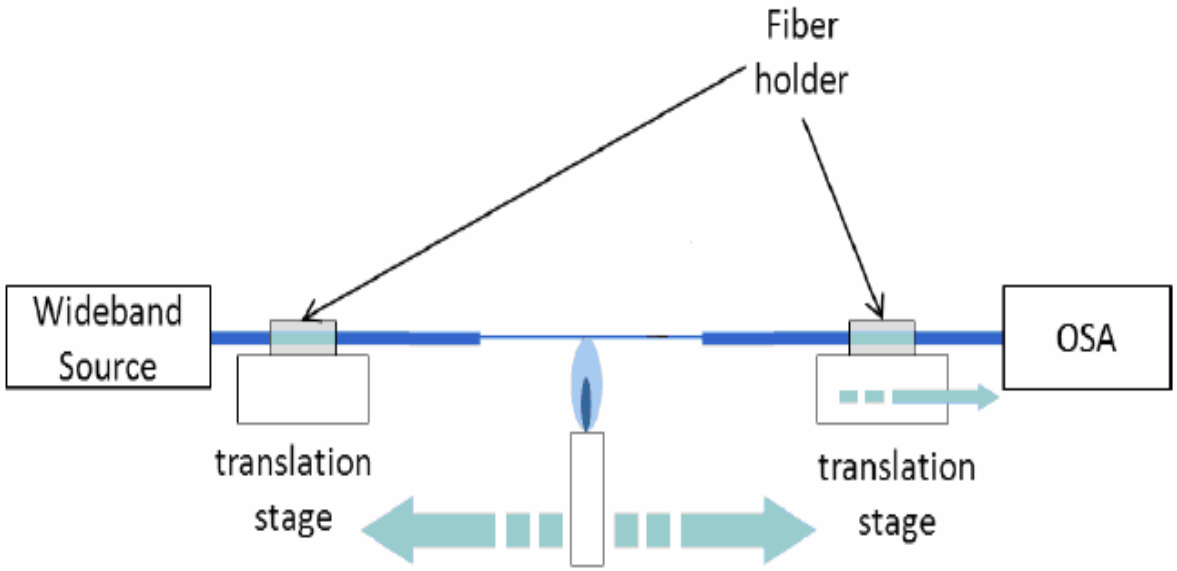

Figure 1.5 – A typical setup for tapered fiber fabrication [11].
OSA, optical spectrum analyzer

First, several centimeters of the optical fiber coating is removed (before the tapering process) and the uncoated segment of the fiber is cleaned thoroughly. Then the fiber is placed horizontally on the translation stage and held by two fiber holders. During the tapering process, a heating source heats the uncoated part of the fiber, while both fiber sides are being pulled apart with constant and equal speeds so as to provide a uniform heat along the fiber (which, in turn, determines the shape and quality of the resulting taper). In order to monitor

the transmission spectrum of the fiber during the process of tapering, a light source is used at one end of the fiber, whereas its other end is connected to the optical spectrum analyzer (OSA). [11, 12]

1.5. D-shaped fiber

1.5.1. D-shaped fiber structure

A D-shaped fiber is a fiber which has a D-shaped segment (see Figure 1.6) along its length.

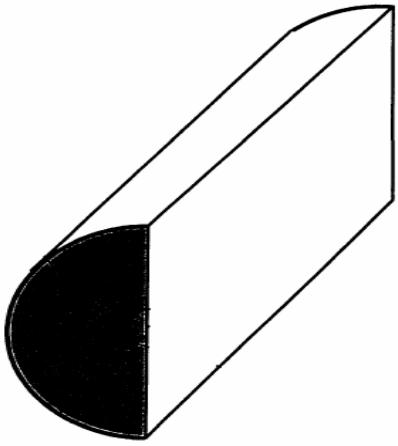

Figure 1.6 – A D-shaped segment.

A flat interface formed by this shape allows optical field emission out of the fiber. Thus, it is based on the same sensing principle as a tapered fiber: interaction of the evanescent field of the surface of a D-shaped fiber with the external environment leads to the attenuation in optical light transmission and the refractive index of the external environment can, therefore, be measured by detecting the transmitted power changes. [13]

1.5.2. D-shaped fiber fabrication

The most common way to produce a D-shaped fiber is by polishing a side of a standard cylindrical optical fiber. This method is relatively simple and fast. Also, it allows a certain amount of flexibility as for the geometry of the D-shaped fiber exposed area. On the other hand, the possibility of some fiber deformations (for example, cracks, scratches or broken regions) cannot be excluded. Thus, very careful attention is required during the process of polishing. [14]

1.6. Plastic optical fiber

Plastic optical fiber (POF) is made of polymer. Usually, POF consists of a polymethylmethacrylate (PMMA), which is also known as acrylic or acrylic glass, core and a

fluoropolymer cladding material. Typically, their refractive indices are ~1,49 and ~1,41 respectively (but the values can vary slightly).

Because of high attenuation, PMMA fibers are mainly used for low-speed and short-distance (up to 100 meters) applications in digital appliances and networks.

Their low cost and high mechanical flexibility allow to use them for sensing purposes. POF are robust under stretching and bending, which is their main advantage over the glass optical fibers.

2. Computer simulations in the BeamPROP software

Modelling of optical fiber structures for detection of liquids with refractive index higher than 1,45 was carried out in the BeamPROP software (which is integrated into the Synopsys CAD environment). This simulation engine uses advanced finite-difference beam propagation (BPM) techniques.

Since BeamPROP does not allow to follow signal spectrum, the sensor is supposed to be used for following the signal intensity. In the simulations all fiber modes are considered. Therefore, in the simulation model the structures were evaluated as ten times smaller ones (in all dimensions in order to save the ratio of the structure cross size to its longitudinal one) to prevent the simulation process from being excessively time-consuming.

2.1. Tapered fiber model

Figure 2.1 illustrates a 3D structure of the biconical taper which was studied in this computer simulation.

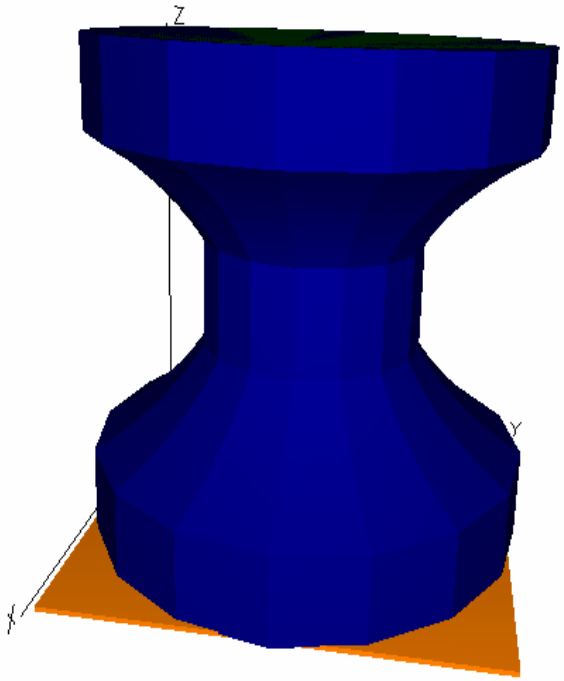

Figure 2.1 – A 3D tapered fiber model.

The structure's longitudinal section view is presented in Figure 2.2. A green part of the structure represents an optical fiber core and a blue one represents its cladding.

In the simulation untapered part diameters of the cladding and core were 50 and 48 μm and the taper surrounding represented liquid.

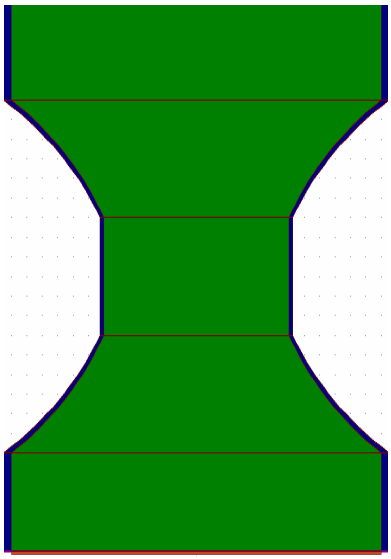

Figure 2.2 – A tapered fiber structure
(longitudinal section view).

The core/cladding refractive indices were 1,491 and 1,405 respectively (see Figure 2.3) so as to correspond to the RI values of the plastic optical fiber used for the sensor structure fabrication (see 3.1.).

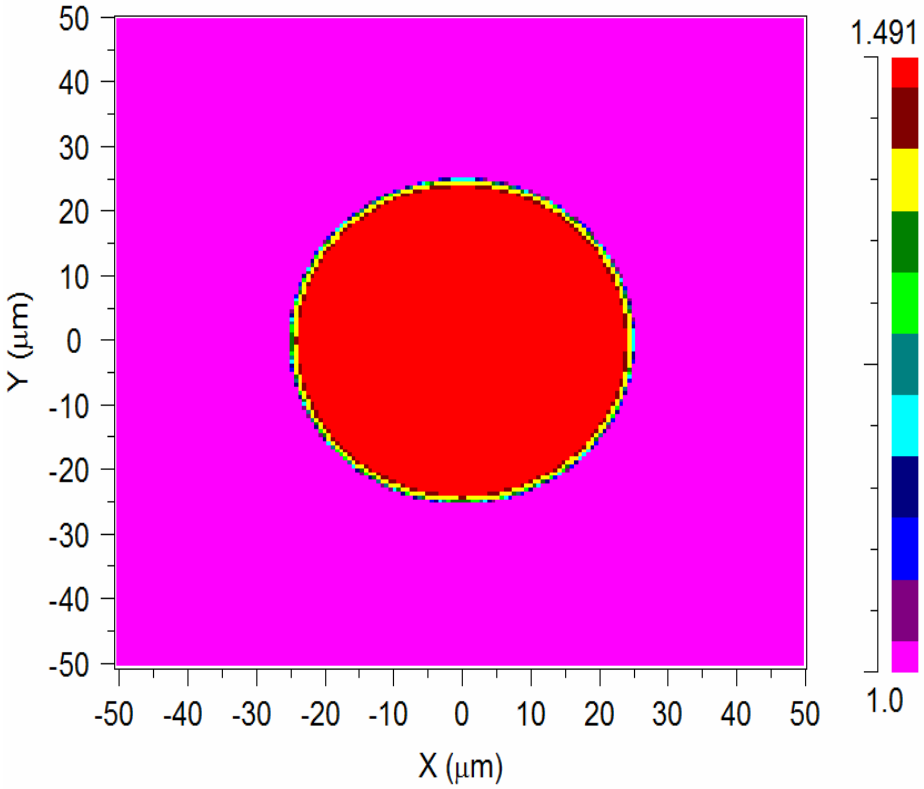

Figure 2.3 – A refractive index profile within a tapered fiber structure
(transverse cross-sectional view).

The subject of interest was the size of the tapered fiber along the *Z*-axis (which was the axis of the light propagation), i.e. the length of the transition segment and the waist, as well as the waist diameter.

First, a "proper" waist diameter was estimated. It means such a diameter that insures sufficient dynamic range of the sensor in order that liquid samples of different refractive indices could be distinguished. In this simulation the taper parameters were as follows: the transition part length and the waist length were 500 μm, the transition part shape was exponential. The source wavelength was set to 1550 nm (which also helped in reducing the simulation time). The waist diameter changed in a ratio of 1:2, 1:3 and 1:4 to the untapered part diameter.

The next figure shows rough estimations (the liquid refractive index changed from 1,451 to 1,486 with a step of 0,005) of this simulation part.

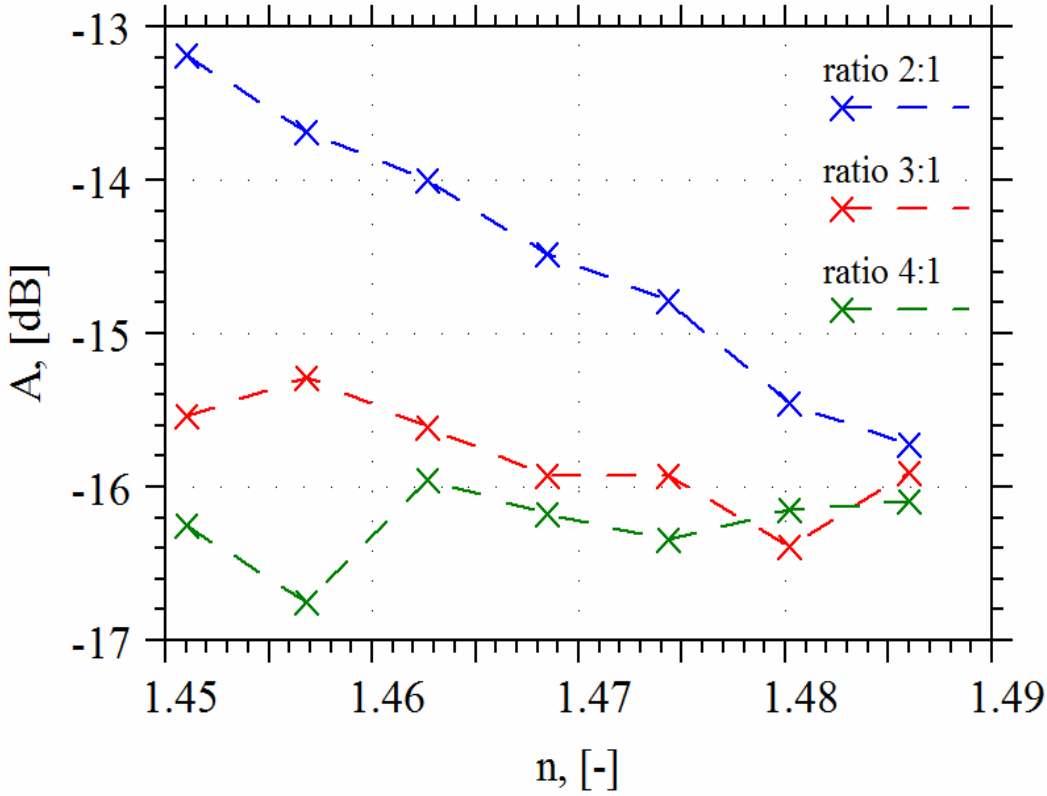

Figure 2.4 – Transfer functions of the tapered fiber structure depending on liquid refractive index changes for different tapering ratios.

As can be observed from Figure 2.4, the best transfer function is the one which corresponds to the tapering ratio 2:1, or to the waist diameter of 25 μm. This characteristic is monotonic (with a tendency to decline with the growing RI) within the whole range of liquid refractive indices as the transmitted power decreases gradually.

Apparently, the structures of higher ratios could not be used for liquid detection purposes at the refractive index range over 1,45 because their characteristics are not sensitive to the refractive index changes.

Then rough estimations of the transfer functions for different taper transition part lengths were carried out (see Figure 2.5).

In this simulation the taper waist diameter was 25 μm, the taper waist length was 500 μm, the transition part shape was exponential. The transition segment length was the variable parameter. Again, the liquid refractive index changed from 1,451 to 1,486 with a step of 0,005.

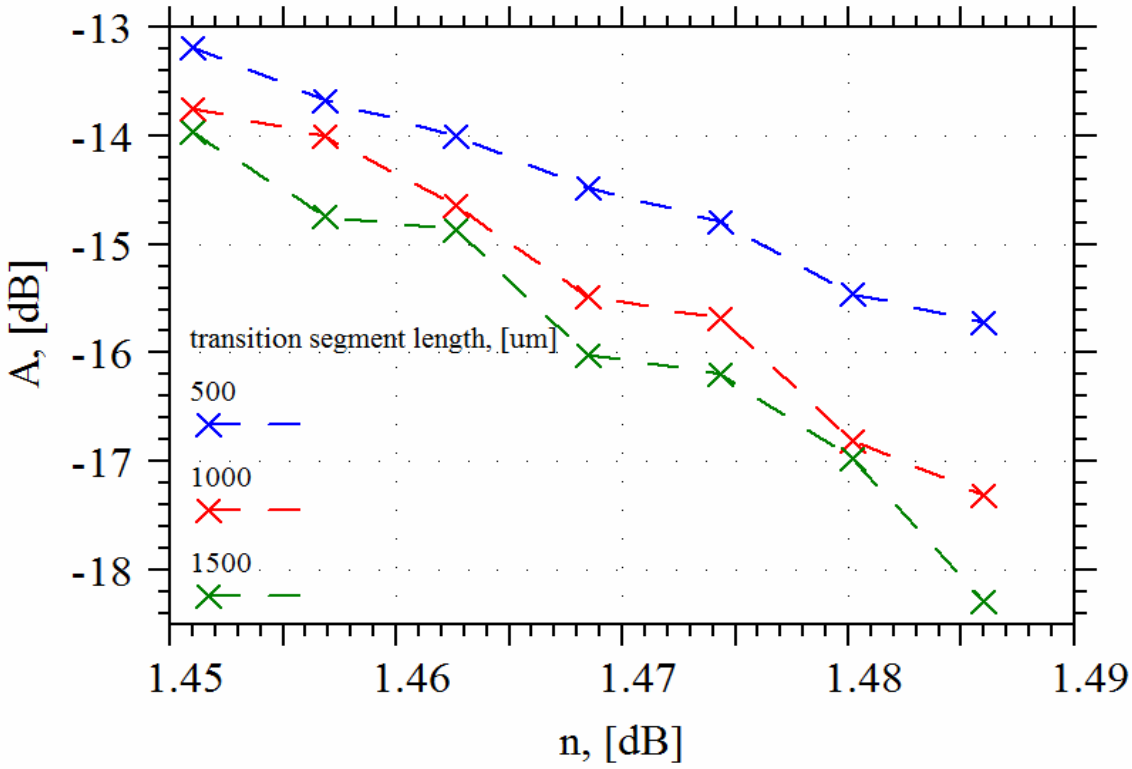

Figure 2.5 – Transfer functions of the tapered fiber structure depending on liquid refractive index changes for different transition segment lengths.

According to the obtained results, transmission loss grows with the increasing of the transition part length. On the other hand, for the taper transition segment length of 500 μm the characteristic is smooth within the whole range of liquid RI, which is good for using a taper for sensing purposes.

The taper waist part length has the same impact on a taper as for the transmission loss (see Figure 2.6).

In this simulation the taper waist diameter was 25 μm, the transition part length was 500 μm, the transition part shape was exponential. The waist length was the examined parameter. The liquid refractive index changed from 1,451 to 1,486 with a step of 0,005.

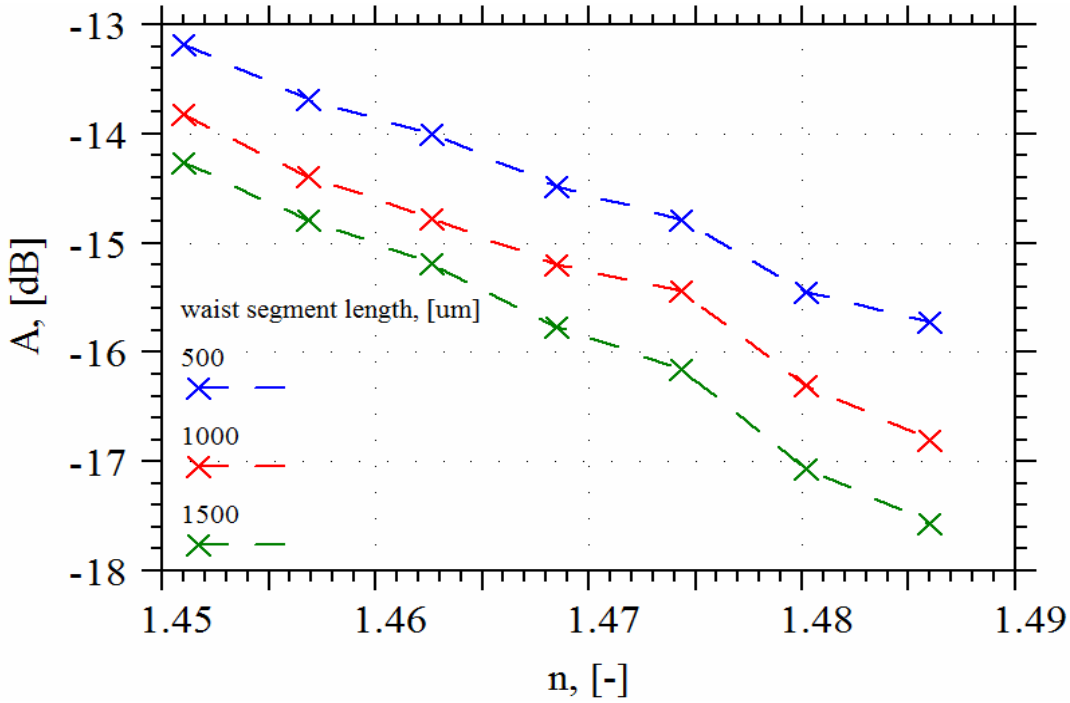

Figure 2.6 – Transfer functions of the tapered fiber structure depending on liquid refractive index changes for different waist segment lengths.

Thus, the final parameters of the proposed tapered fiber are as follows: the transition part and the waist part lengths are 500 μm and 1500 μm respectively (which corresponds to 0,5 cm and 1,5 cm for the real one – technologically, it can be fabricated), the waist diameter is 25 μm (or 250 μm for the real one).

For the taper with the above-mentioned parameters its transfer function was studied in more detail. In this simulation the RI changed from 1,451 to 1,486 with a step of 0,0035.

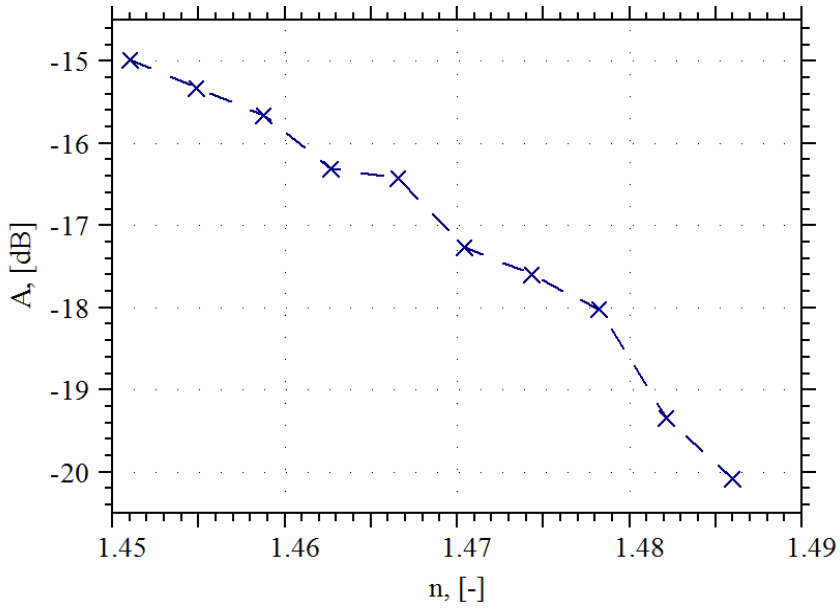

Figure 2.7 – Transfer function of the proposed tapered fiber structure depending on liquid refractive index changes.

2.2. D-shaped fiber model

The next computer simulation part included a model of a D-shaped fiber (see its 3D structure in Figure 2.8).

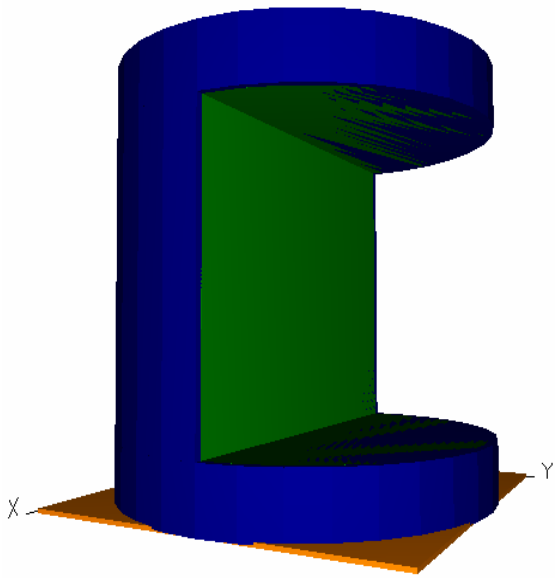

Figure 2.8 – A 3D structure of a D-shaped fiber model.

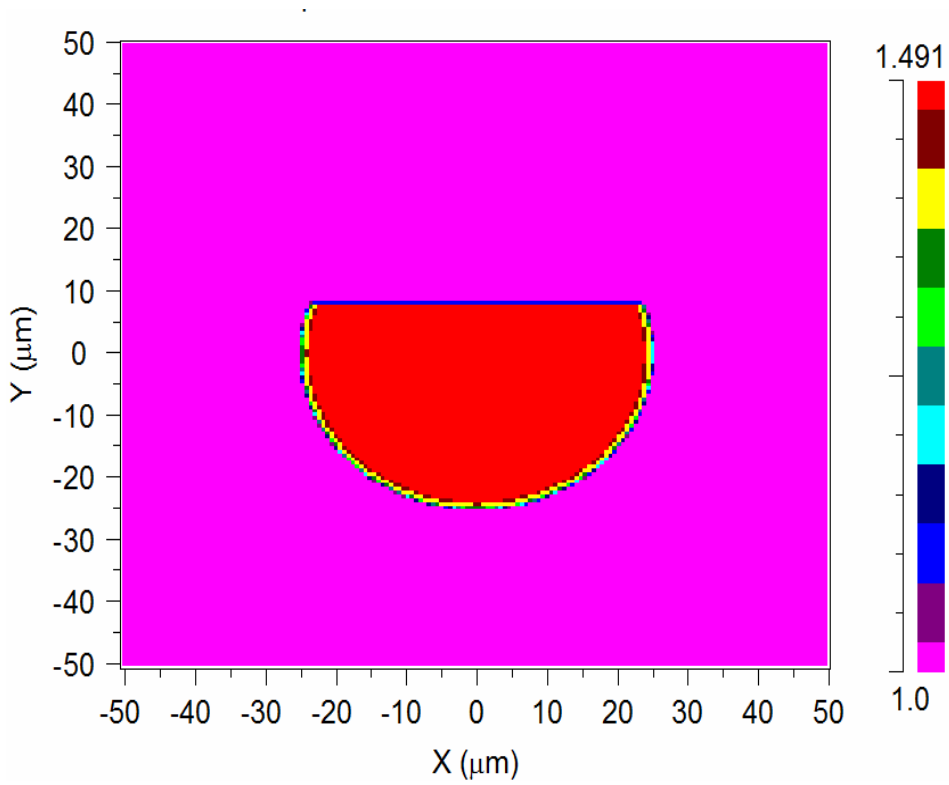

Figure 2.9 – A refractive index profile within a D-shaped structure (transverse cross-sectional view).

In this case the polished segment depth and length were the subject of interest. Similar approach as in 2.1. was used in order to find them. First, a polished part depth influence of the D-shaped fiber model on the transfer function was estimated.

In this simulation part the polished segment length was 1000 μm. The source wavelength was set to 1550 nm. The polished segment depth was set to *R*/3, 2*R*/3 and *R* (where *R* is an optical fiber radius).

The next figure shows rough estimations (the liquid refractive index changed from 1,451 to 1,486 with a step of 0,005) obtained in this computer simulation.

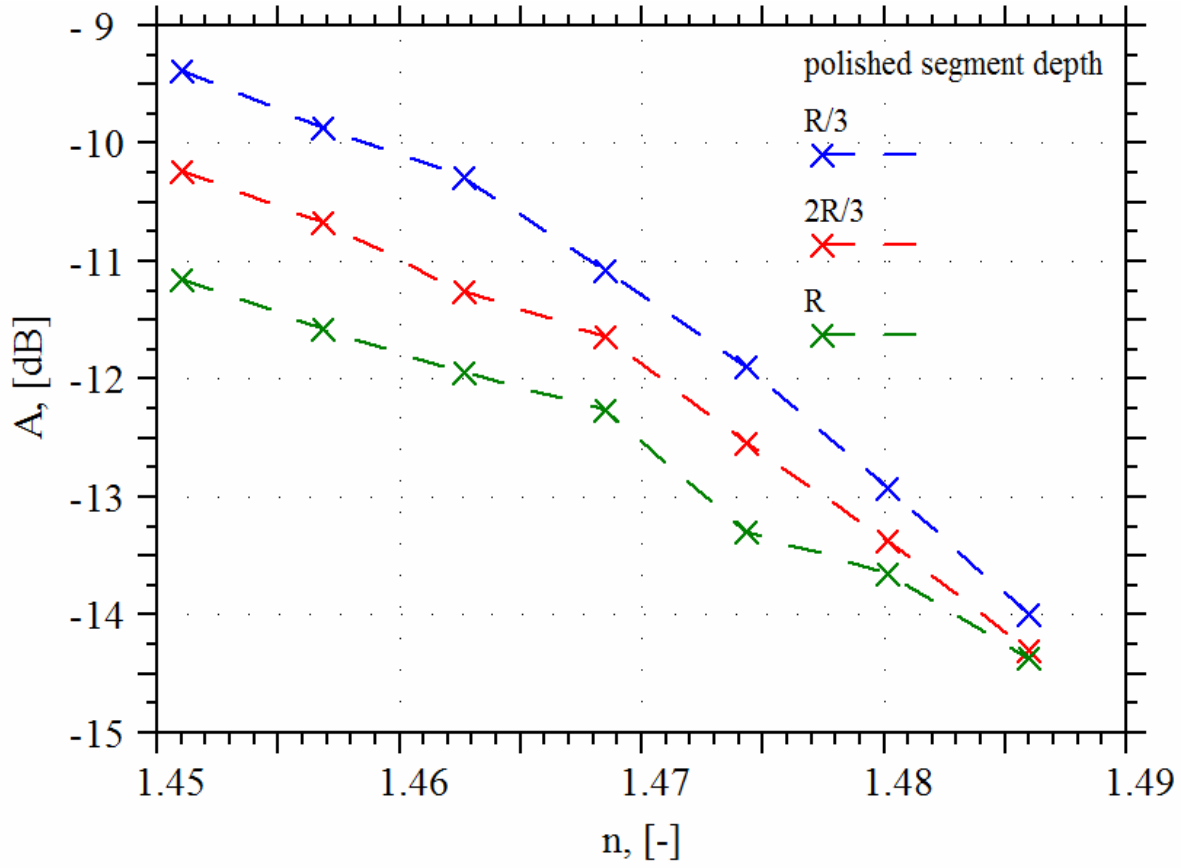

Figure 2.10 – Transfer functions of the D-shaped fiber structure depending on liquid refractive index changes for different polished segment depths.

As might be seen from the obtained results, the best transfer function is the one which corresponds to the polished segment depth of *R*/3. This characteristic has a sharper slope (which increases the sensor sensitivity) in comparison with the remaining characteristics and it decreases more monotonously (is smoother) within the whole range of liquid refractive indices.

Then rough estimations of the transfer functions for the polished segment depth of *R*/3 and different polished part lengths were carried out (see Figure 2.11).

In this simulation part the liquid refractive index changed from 1,451 to 1,486 with a step of 0,005.

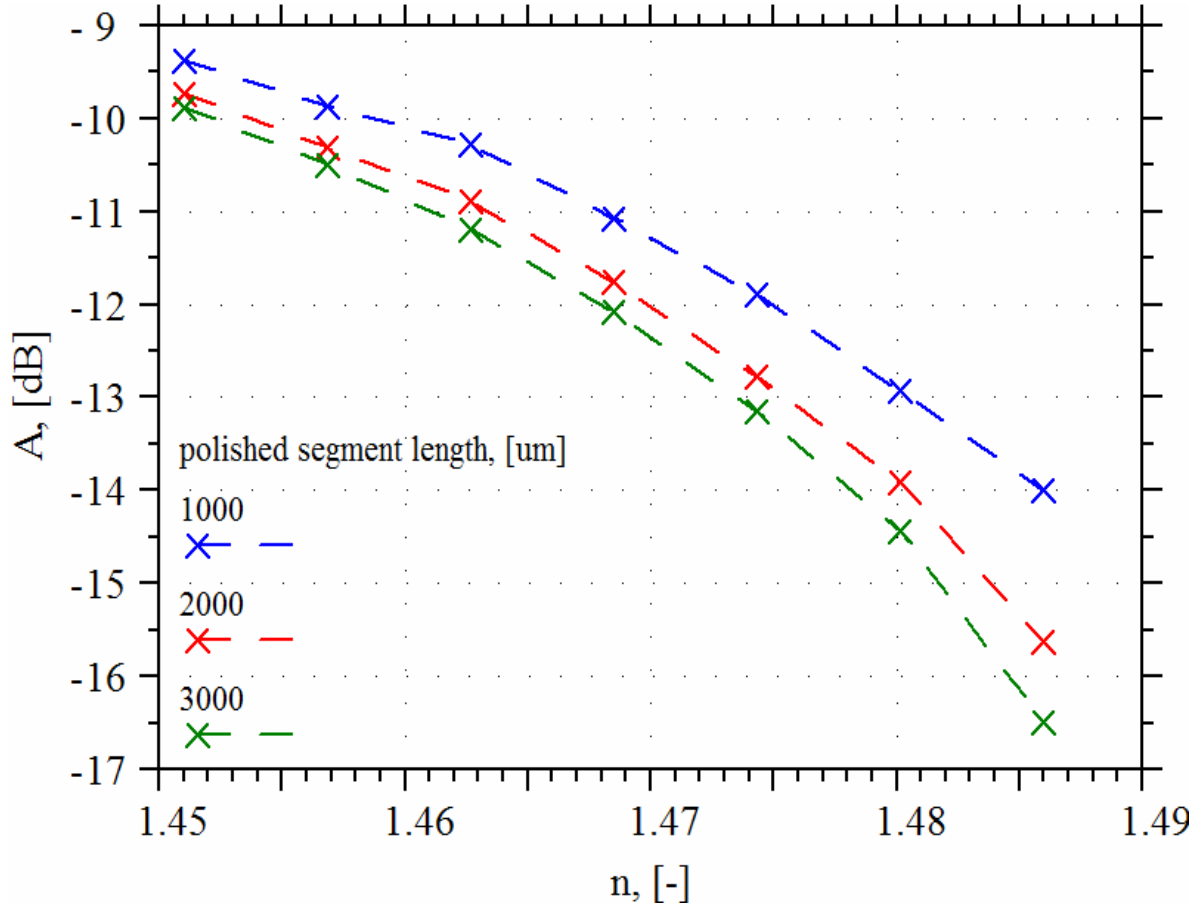

Figure 2.11 – Transfer functions of the D-shaped fiber structure depending on liquid refractive index changes for different polished segment lengths.

According to expectations and similarly to the results from Figure 2.6 for a tapered fiber structure, transmission loss grows with the increasing of the polished part length. For the polished segment length of 3000 μm the decrease of the characteristic is sharper (which again increases the sensor sensitivity).

The final parameters of the proposed D-shaped fiber are as follows: the polished segment depth is $R/3$ and the polished segment length is 3000 μm (which corresponds to 3 cm for the real structure).

For the D-shaped fiber model with the above-mentioned parameters its transfer function was studied in more detail (see Figure 2.12).

In this simulation the liquid refractive index changed from 1,451 to 1,486 with a step of 0,0035.

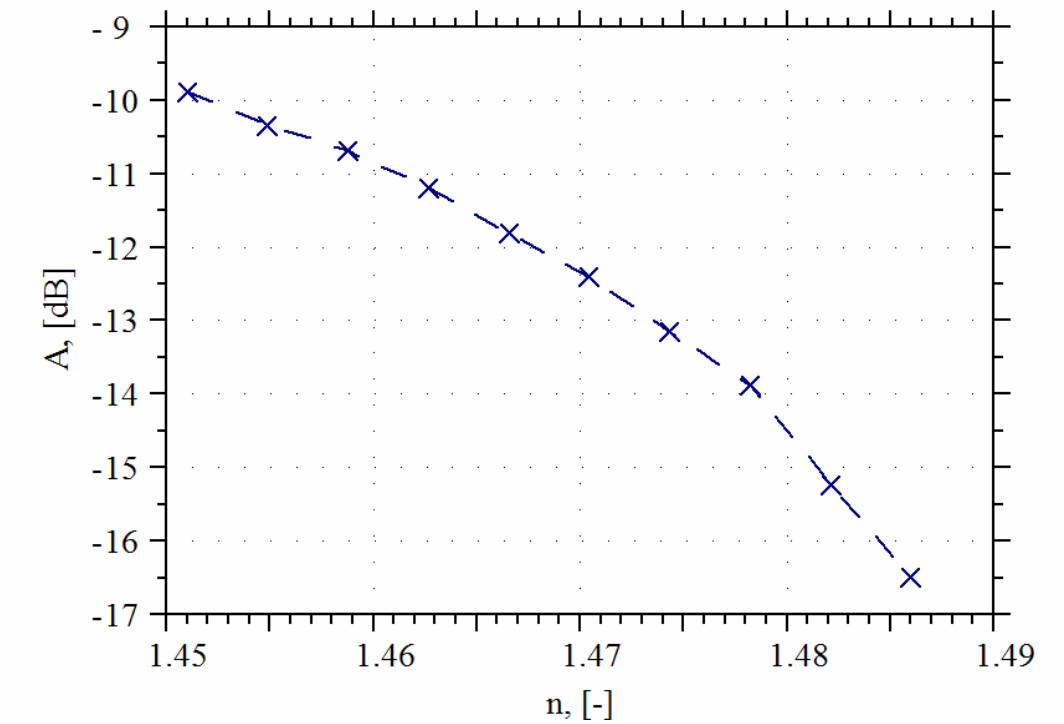

Figure 2.12 – Transfer function of the proposed D-shaped fiber depending on liquid refractive index changes.

As follows from Figure 2.12, the trunsfer function of the proposed D-shaped fiber is similar to the one obtained for the proposed tapered fiber structure (see Figure 2.7). However, here an obvious advantage is that the characteristic is smooth within the whole range of liquid refractive indices.

3. A measurement setup realization

In the same way as it was in the simulations, in the measurements the sensor structures were used for following the signal intensity. A setup scheme for carring out the measurements is presented below (see Figure 3.1), as well as all the units used for the setup are described.

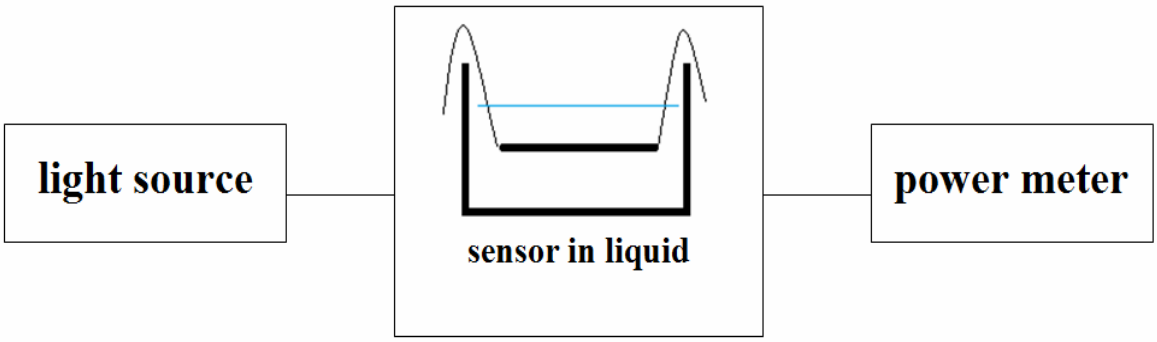

Figure 3.1 – A measurement setup scheme.

3.1. POF chosen for the measurements

In the project a standard POF of 486/500 μm core/cladding diameter by LEONI Fiber Optics, Inc. was chosen for the measurements. This fiber is flexible enough (in comparison with POF of 980/1000 μm core/cladding diameter) to be used as U-shape sensor structure (see 4.2.). In addition to it, it is thick enough to be polished (in order to prepare a sensor structure) under existing (not professional) laboratory conditions.

The fiber consists of a super pure PMMA core and fluoropolymer cladding. Its numerical aperture (NA) is 0,5. [15]

With the core refractive index of ~1,491 the cladding refractive index of the fiber is then:

$$n_{cl} = \sqrt{n_{core}^2 - NA^2} = \sqrt{1{,}491^2 - 0{,}5^2} \approx 1{,}405 \qquad (3.1)$$

For the 9,2-meter long POF its transmission characteristic as a function of wavelength was measured (see Figure 3.2).

It approximately corresponds to the description in datasheet (see [15]): the working range of the fiber belongs to the visible wavelength one and within it the characteristic has a relative attenuation maximum at a wavelength of ~625 nm. It determines the choice of light sources for POF.

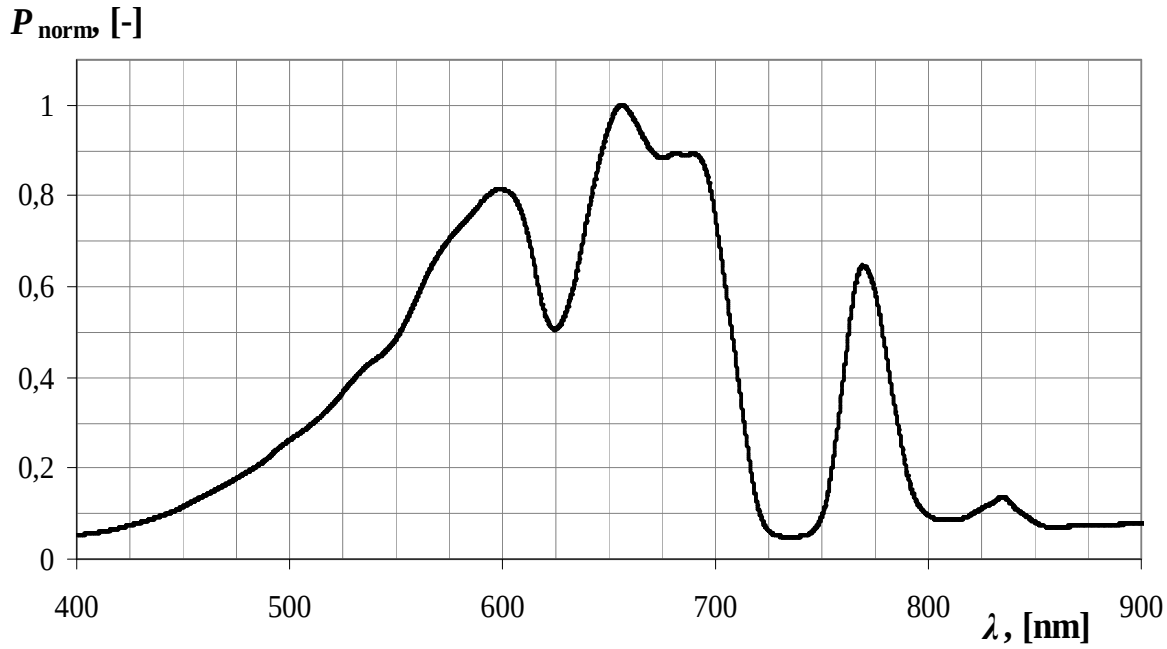

Figure 3.2 – Normalized transmitted power as a function of wavelength of the 9,2-meter long POF.

Based on the obtained transmission characteristic, the POF attenuation α in dB/km was calculated for its working range (see Figure 3.3).

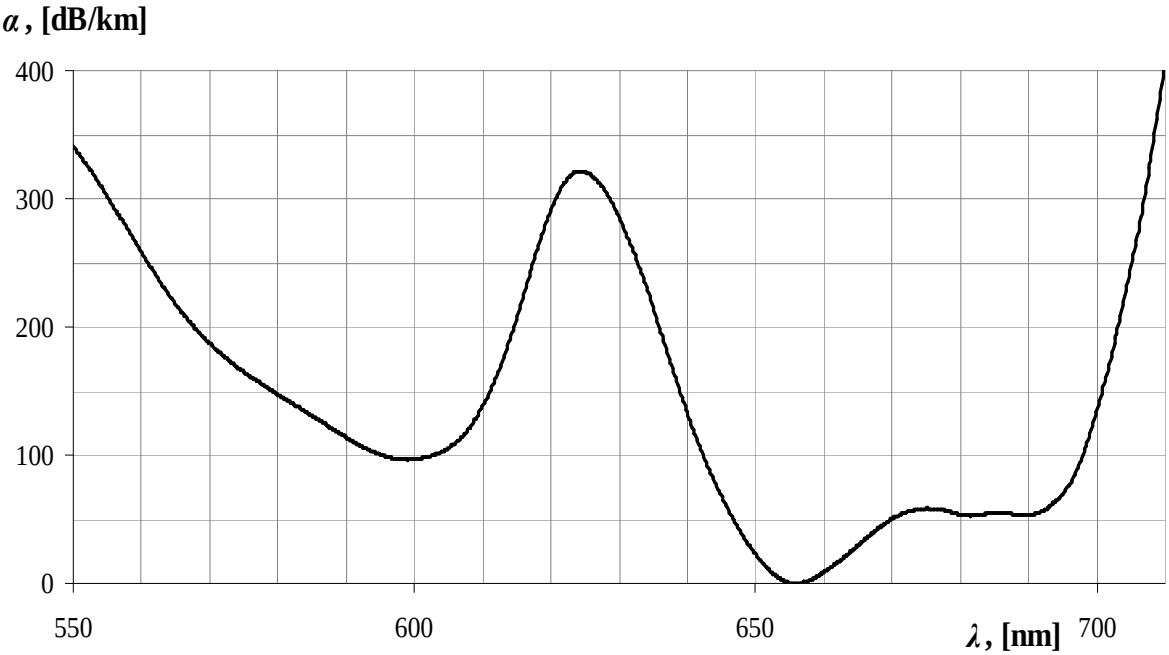

Figure 3.3 – Attenuation as a function of wavelength of the chosen POF.

3.2. A light source

HL-2000-FHSA (halogen light source with filter holder/shutter and attenuator) by Ocean Optics, Inc. was used as a light source. Its spectral emission includes visible wavelengths, which is appropriate for POF chosen for the measurements. [16, 17]

3.3. A power meter

So as to detect the power, *PM100D* (Compact Power and Energy Meter Console) with *S121C* photodiode sensor/detector by Thorlabs, Inc. was used. Its wavelength range and power range are 400-1100 nm and 500 nW-500 mW respectively. [18, 19]

3.4. Connectors

In order to connect the fiber with the light source and the power meter two Bare Fiber Terminators *BFT1* with *B10510A* Multimode SMA905 Connectors by Thorlabs, Inc. were used. [20]

3.5. A measurement setup

Thus, when all the required units and components were prepared, the measurement setup was made (see Figure 3.4).

Figure 3.4 – A measurement setup.

3.6. Liquid analytes

Liquids under test were prepared as mixtures of water and glycerol anhydrous (C3H8O3), which is colorless, odorless and, most importantly, non-toxic.

The refractive index of glycerol was 1,47126. As it was the highest possible refractive index to measure, it limited the measurements from the point of view that not all working range of the D-shaped fiber could be tested (not to the value of ~1,49 as it was done in the simulation part of the work).

Three mixtures of different refractive indices were prepared for the measurements so as to be approximately of the same step within the range of 1,45 to 1,47126. In two weeks, when the liquids were mixed enough, there refractive indices were measured by a refractometer. The results were 1,45027, 1,45721 and 1,46336.

3.7. Fabrication of a D-shaped sensor structure

Since it was not possible to fabricate a tapered FOS structure because of the available equipment, a D-shaped one was prepared for the experimental part. The process of its preparation was as follows.

A metal V-groove was used for polishing the POF. It allowed to fix the fiber position and to prevent its rotation. In addition to it, the V-groove is resistant to the polishing material. The fiber was placed in the groove and held by two magnets in order to fix it immovable. As the V-groove is designed for smaller fibers than the chosen POF's thickness/diameter, upper part of the POF was above the metal surface. Thus, it allowed to polish this exposed side of the fiber, which was done with the help of diamond lapping/polishing sheets *LFxD* [21] by Thorlabs, Inc. Figure 3.5 represents the fiber before (left side) and after (right side) the polishing (when some energy is radiating out of the polished segment). The polished part was 3 cm long.

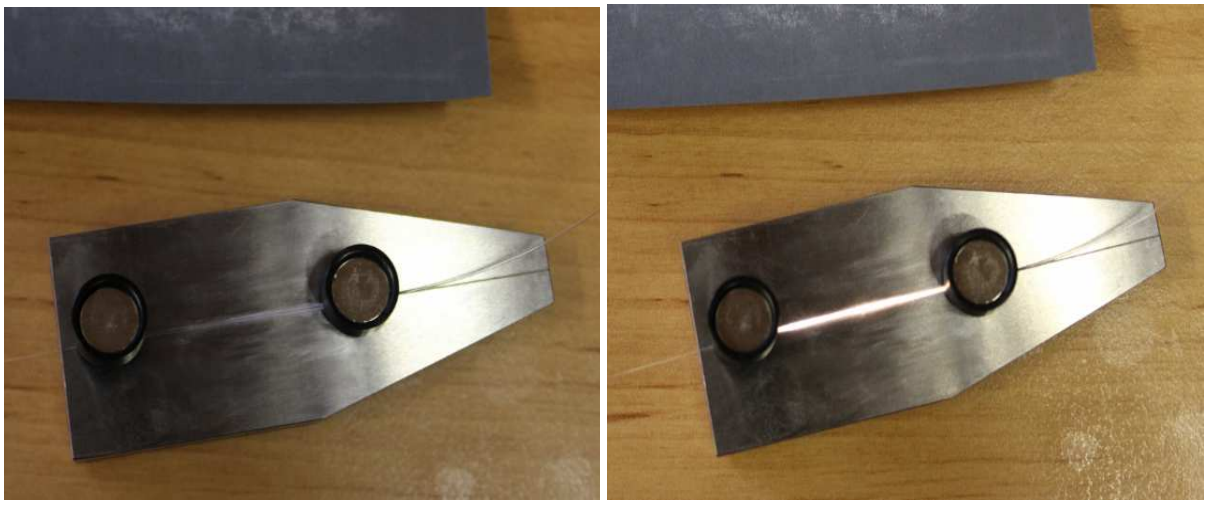

Figure 3.5 – A D-shaped sensor structure fabrication.

Transverse cross-sectional views of the unpolished POF and the fiber after the polishing observed under microscope are also shown in Figures 3.6 and 3.7 respectively.

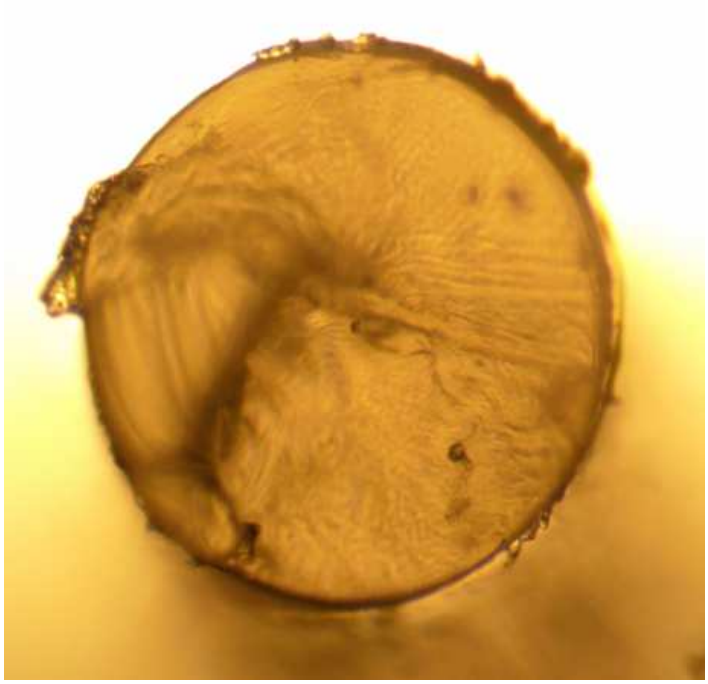

Figure 3.6 – An unpolished POF observed under microscope (transverse cross-sectional view).

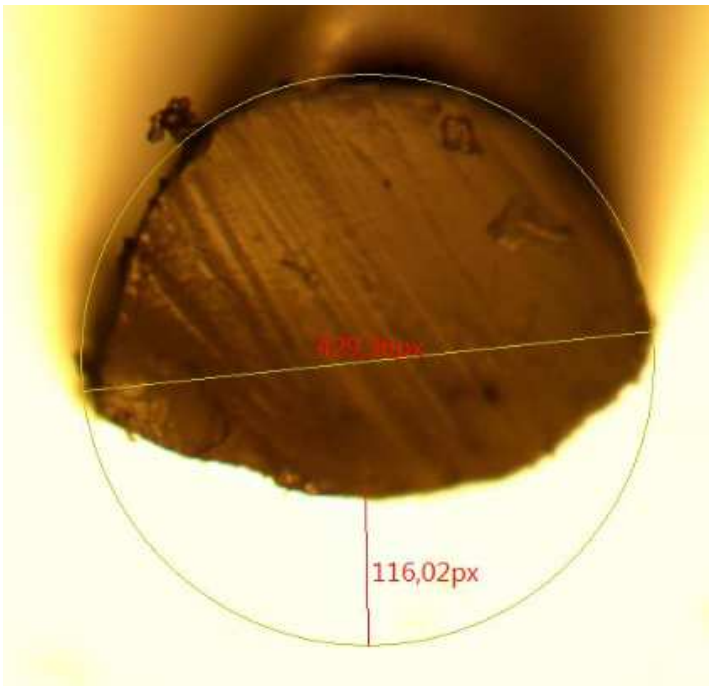

Figure 3.7 – A D-shaped sensor structure observed under microscope (transverse cross-sectional view).

As the polishing process was done manually, the polishing was not ideal. It was not possible to follow/regulate the polishing segment depth. Therefore, it was not constant in both, transverse and longitudinal directions. In the longitudinal direction the polished part depth

changed gradually from the value of ~42 μm at the D-shaped segment edges to the value of ~135 μm, where the D-shaped segment was the thinnest.

On having fabricated the sensor structure, its transmission loss in the air was measured. For this purpose, an unprocessed POF part of the same length (60 cm) as the one with the sensor structure was used. According to the scheme from Figure 3.1 the output power was measured for both of the fibers (with the same power of the light source). The difference (and so the transmission loss) was ~12,6 dB.

4. Experimental campaign

All the measurements described below were carried out for the same measurement setup (according to Figure 3.1). The only difference was the structure of the sensor used during the measurements.

4.1. Measurements with the unbent sensor structure

First, measurements with the prepared D-shaped fiber of its original form (unbent) were made. Before the measurements, the sensor was cleaned thoroughly with isopropyl alcohol (IPA) so as to remove impurities and then it was dried. The light source was tuned in such a manner that the value of the detector was -10 dBm (this value was considered to be the reference one in all the measurements).

Then, the sensor was immersed into the liquid sample 1 (with the refractive index of 1,45027) and the output power *P* was measured. The process was repeated ten times (for the same liquid sample) in order to verify the measurement repeatability.

Afterwords, the sensor was again purified with IPA and dried so as to be prepared for the measurements with the liquid sample 2 (with the refractive index of 1,45721) and the light source was tuned for the reference value on the power meter.

The measurement process was the same as above described (and for all the remaining liquid samples). The results of this set of measurements are presented in Table 4.1.

Table 4.1: Results of the measurements with the unbent sensor structure.

	liquid refractive index ***n*, [-]**			
	1,45027	1,45721	1,46336	1,47126
measurement	***P*, [dBm]**			
1	-11,38	-11,80	-12,35	-13,15
2	-11,41	-11,76	-12,28	-13,08
3	-11,35	-11,77	-12,25	-13,05
4	-11,40	-11,82	-12,30	-13,11
5	-11,36	-11,83	-12,33	-12,99
6	-11,33	-11,79	-12,27	-13,04
7	-11,41	-11,80	-12,30	-13,07
8	-11,33	-11,66	-12,34	-13,10
9	-11,42	-11,79	-12,37	-13,02
10	-11,37	-11,81	-12,42	-13,09

The results from Table 4.1 show that the output power varies with the liquid refractive index changes. According to expectations, the higher the refractive index, the less the output power

(in other words, the transmission loss increases as the refractive index changes from 1,45027 to 1,47126).

4.2. Measurements with U-shaped sensor structures

Then, the flexibility of POF was used to expand the measurements. In order to enhance the evanescent wave (and so to increase the transmission loss) of the sensor, its structure was bent to make a U-shape one (see Figure 4.1).

Figure 4.1 – Examples of bent D-shaped optical fibers [13].

These structures were used with the U-part radius of 6 mm and 4 mm. The less radius was again supposed to enhance the evanescent wave.

The measurement process was the same as described in 4.1. The results of these two sets of measurements are presented in Tables 4.2 and 4.3.

Table 4.2: Results of the measurements with a U-shaped sensor structure with radius of 6 mm.

	liquid refractive index ***n*, [-]**			
	1,45027	1,45721	1,46336	1,47126
measurement	***P*, [dBm]**			
1	-12,37	-13,44	-14,84	-18,47
2	-12,43	-13,39	-14,80	-18,52
3	-12,43	-13,38	-14,73	-18,58
4	-12,51	-13,41	-14,79	-18,65
5	-12,47	-13,34	-14,77	-18,60
6	-12,52	-13,39	-14,80	-18,49
7	-12,38	-13,36	-14,81	-18,61
8	-12,43	-13,42	-14,78	-18,58
9	-12,40	-13,40	-14,72	-18,56
10	-12,38	-13,35	-14,78	-18,53

Table 4.3: Results of the measurements with a U-shaped sensor structure with radius of 4 mm.

	liquid refractive index ***n*, [-]**			
	1,45027	1,45721	1,46336	1,47126
measurement	***P*, [dBm]**			
1	-14,28	-14,90	-16,29	-20,18
2	-14,31	-14,88	-16,30	-20,23
3	-14,25	-14,93	-16,26	-20,21
4	-14,29	-14,91	-16,27	-20,24
5	-14,31	-14,88	-16,31	-20,20
6	-14,32	-14,87	-16,28	-20,25
7	-14,30	-14,85	-16,32	-20,22
8	-14,28	-14,88	-16,29	-20,19
9	-14,27	-14,90	-16,26	-20,21
10	-14,28	-14,87	-16,27	-20,18

As is evident from the obtained results, with the growing liquid refractive index the transmission loss increase for the U-shaped sensor structure is more obvious in comparison with the unbent one and it is higher for the structure with a U-part with radius of 4 mm in comparison with the one with radius of 6 mm.

The results of all the above-mentioned measurements are also described and discussed in 4.4.

4.3. Evaluation of the measurement uncertainty for the obtained data

In order to characterise the dispersion of the output power as the measurand its uncertainty was calculated. Algorithm of the uncertainty calculation is presented below for the set of measurements with the unbent sensor structure and glycerol as a liquid sample. The results for all the other sets of measurements are provided in Appendix.

The initial data for finding the uncertainty are the values P_i (the results of repeated measurements of the output power estimated from N=10 independent observations).

Table 4.4: Data for the uncertainty calculation.

i	1	2	3	4	5	6	7	8	9	10	$\downarrow \overline{P}$
P_i, [dBm]	-13,15	-13,08	-13,05	-13,11	-12,99	-13,04	-13,07	-13,10	-13,02	-13,09	-13,07
P_i, [µW]	48,42	49,20	49,55	48,87	50,23	49,66	49,32	48,98	49,89	49,09	49,32
$P_i - \overline{P}$, [µW]	-0,90	-0,12	0,23	-0,45	0,91	0,34	0,00	-0,34	0,57	-0,23	

For the measurements carried out in the work the standard uncertainty is given by two components: the type A (which is based on statistical analysis of measurement results) and the type B (which includes properties of means – materials and instruments – used for measurements).

The arithmetic mean $\overline{P}$ is defined as the average of N individual values P_i:

$$\overline{P} = \frac{1}{N}\sum_{i=1}^{N} P_i = \frac{1}{10}\sum_{i=1}^{10} P_i = 49{,}32 \text{ [µW]} \tag{4.1}$$

The type A of the standard uncertainty, or the experimental standard deviation of the mean, is then [22, 23]:

$$u_{A(P)} = \sqrt{\frac{\sum_{i=1}^{N}\left(P_i - \overline{P}\right)^2}{N\cdot(N-1)}} = \sqrt{\frac{\sum_{i=1}^{10}\left(P_i - \overline{P}\right)^2}{10\cdot(10-1)}} = 0{,}1672 \text{ [µW]} \tag{4.2}$$

The type B of the standard uncertainty in the measurements was given by the power meter parameters [19]. Its value is [24]:

$$u_{B(P)} = \frac{1}{\sqrt{3}}\left(\frac{\delta\cdot\overline{P}}{100} + D\cdot R_P\right) = \frac{1}{\sqrt{3}}\left(\frac{0{,}03\cdot 49{,}32}{100} + 4\cdot 0{,}01\right) = 0{,}8773 \text{ [µW]} \tag{4.3}$$

where $\overline{P}$ is a measurement value, δ is the power meter accuracy of reading, D is the number of digits and R_P is the power meter resolution.

Then, the expanded combined standard uncertainty for the coverage factor k=2 (which means that the uncertainty defines a range that is expected to contain the true value of the measurement result with the probability of 95%) is calculated as [24, 25]:

$$u_{C(P)} = k\cdot u_{C(P)} = 2\sqrt{u_{A(P)}^2 + u_{B(P)}^2} = 2\sqrt{0{,}1672^2 + 0{,}8773^2} = 1{,}79 \text{ [µW]} \tag{4.4}$$

or the combined standard uncertainty in units of dBm is [23]:

$$u_C = \left|\left[10\cdot\log\left(\overline{P}\right)\right]\right|\cdot u_{C(P)} = 10\cdot\frac{u_{C(P)}}{\overline{P}\cdot\ln(10)} = 10\cdot\frac{1{,}79}{49{,}32\cdot\ln(10)} = 0{,}16 \text{ [dBm]} \tag{4.5}$$

The final result is then: P = -13,1 dBm ± 0,2 dBm

4.4. Results and discussion

For all three sets of measurements the normalized output power (with regard of the reference value of -10 dBm) for different liquid refractive indices was calculated (see Table 4.5 and Figure 4.2).

Table 4.5: The normalized output power for the measured sensor structures.

	liquid refractive index ***n*, [-]**			
	1,45027	1,45721	1,46336	1,47126
sensor structure	$\overline{P}_{norm}$**, [dB]**			
unbent	-1,4	-1,8	-2,3	-3,1
U-shaped of R = 6 mm	-2,4	-3,4	-4,8	-8,6
U-shaped of R = 4 mm	-4,3	-4,9	-6,3	-10,2

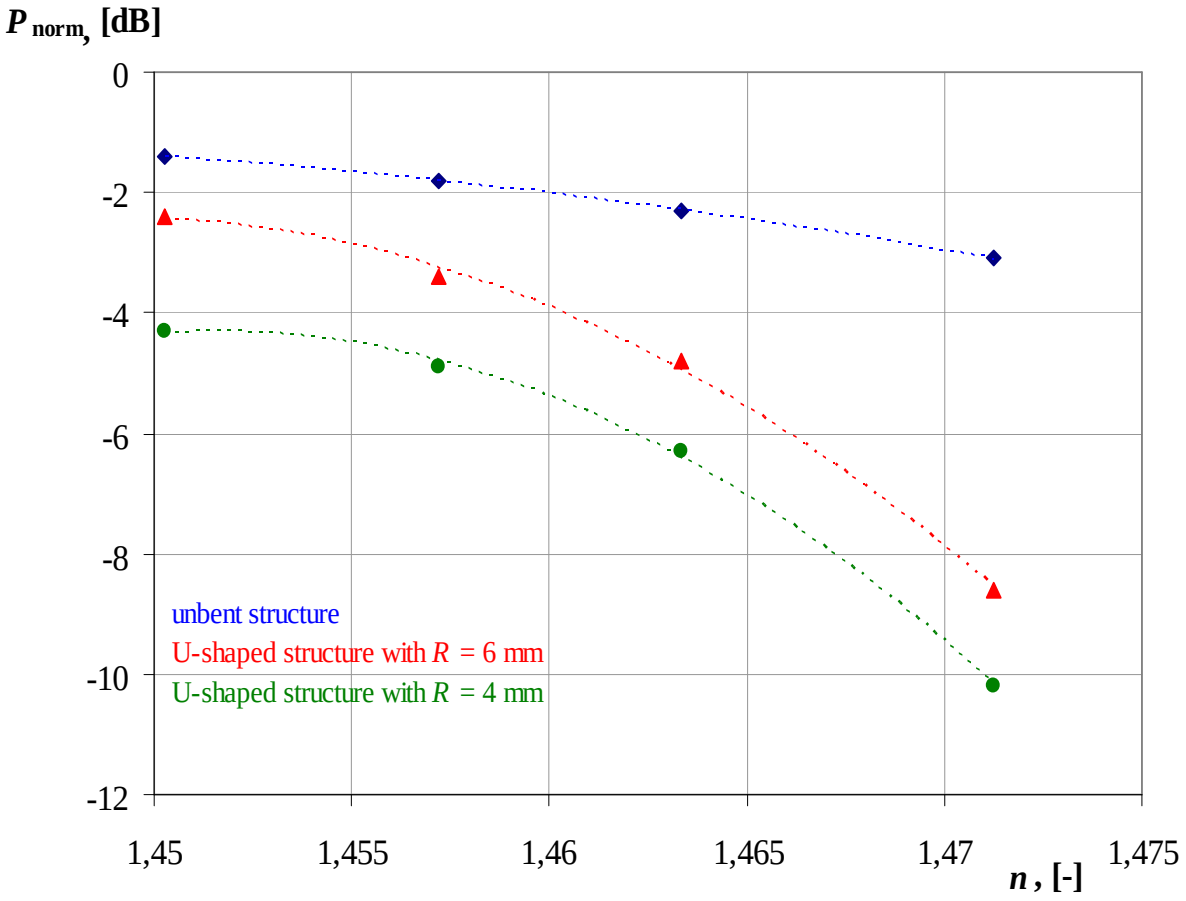

Figure 4.2 – Transfer functions of the measured D-shaped sensor structures depending on liquid refractive index changes.

As can be observed from Figure 4.2, the experimental results for the unbent sensor structure approximately correspond to those obtained from the simulations (see Figure 2.12). Transmission loss increases slowly with the refractive index growth. A certain discrepancy in different slopes of these two characteristics can be caused by the defects of the real D-shaped sensor structure which were mentioned in 3.2.

The U-shaped structures allowed to obtain the better sensitivity of the sensor. According to expectations, the best result was for the U-shaped structure with radius of 4 mm: in the refractive index range from 1,46336 to 1,47126 it reached the value of 493,7 dB/RIU (see Table 4.6).

Table 4.6: Sensitivity of the measured sensor structures (in dB/RIU).

sensor structure	liquid refractive index range		
	1,45027 – 1,45721	1,45721 – 1,46336	1,46336 – 1,47126
unbent	57,6	81,3	101,3
U-shaped of R = 6 mm	144,1	227,6	481
U-shaped of R = 4 mm	86,5	227,6	493,7

The example of the sensor sensitivity calculation (for the U-shaped structure of R = 4 mm and the refractive index range of 1,46336 – 1,47126):

$$S = \frac{\Delta \overline{P}_{norm}}{\Delta n} = \frac{\left|-10{,}2-(-6{,}3)\right|}{1{,}47126-1{,}46336} \approx 493{,}7 \ \text{[dB/RIU]} \tag{4.5}$$

There is an obvious difference between the results for the same sensor structures for different refractive index ranges. It can be explained by a poor linearity of the characteristics, which is a certain disadvantage of the sensor. The transmission loss increase is more rapid for higher refractive indices.

Also, for the sensor structures their resolution was calculated (see Table 4.7), which is the minimum refractive index change that can be indicated by a sensor. Resolution can be defined as follows [26, 27]:

$$Res = \frac{u_C}{S} \tag{4.6}$$

where u_C is a standard deviation (see 4.3.) and S is the sensor sensitivity.

Table 4.7: Resolution of the measured sensor structures.

sensor structure	liquid refractive index range			***average***
	1,45027 – 1,45721	1,45721 – 1,46336	1,46336 – 1,47126	
unbent	$3{,}47 \cdot 10^{-3}$	$2{,}46 \cdot 10^{-3}$	$1{,}97 \cdot 10^{-3}$	$2{,}63 \cdot 10^{-3}$
U-shaped of R = 6 mm	$1{,}39 \cdot 10^{-3}$	$0{,}88 \cdot 10^{-3}$	$0{,}42 \cdot 10^{-3}$	$0{,}90 \cdot 10^{-3}$
U-shaped of R = 4 mm	$2{,}31 \cdot 10^{-3}$	$0{,}88 \cdot 10^{-3}$	$0{,}41 \cdot 10^{-3}$	$1{,}2 \cdot 10^{-3}$

Logically, the best resolution was again for the U-shaped sensor structure with radius of 4 mm for the RI range of 1,46336 – 1,47126.

Conclusion

In this master's thesis the detection of liquids using plastic optical fibers was studied. The focus was on optical sensing based on the refractometric principle utilizing evanescent wave with the emphasis on liquids of the refractive indices higher than the refractive index of fused silica.

The theoretical results (based on analyses in a computer simulation environment for a set of liquids of the refractive index range over 1,45) included proposed sensor structures for the follow-up measurements.

In the practical part of the work several sensor structures were prepared and measurements were carried out with them. Data obtained from the experiments confirmed theoretical assumptions and also showed some sensor structure properties (sensitivity, resoluton) which could affect liquid detection.

Taking into account that the fabricated sensor structure was not perfect because of certain defects due to the conditions under which it was made, there is room for further improvement of the results. Nevertheless, judging from the work, sensors based on POF, could be expected to find their applications in liquid detection owing to their low cost, high sensitivity and reliability.

References

[1] Vivek Alwayn: *Optical Network Design and Implementation*. Cisco Press, March 17, 2004. Available from: http://www.ciscopress.com/articles/article.asp?p=170740&seqNum=5

[2] *Fiber Optic Basics.* Tutorial. Available from: https://www.newport.com/t/fiber-optic-basics

[3] Deepak Kumar, P. K. Chroudhury: *Introduction to modes and their designation in circular and elliptical fibers*. Faculty of Engineering, Multimedia University, Cyberjaya 63100, Malaysia, February 2, 2007. Available from: http://www.ugcfrp.ac.in/images/userfiles/68227-Deepakpaper-9.pdf

[4] M. Zourob, A. Lakhtakia: *Optical Guided-wave Chemical and Biosensors II.* Heidelberg: Springer, 2010, 301 pages.

[5] *Intensity modulation sensors: examples and applications.* Optics 4 engineers: Online Cources. Available from: http://www.optique-ingenieur.org/en/courses/OPI_ang_M06_C04/co/Grain_OPI_ang_M06_C04_2.html

[6] Ginu Rajan: *Optical Fiber Sensors: Advanced Techniques and Applications.* CRC Press, March 2, 2015, 575 pages.

[7] John Hanson: *Refractometry.* 2003. Available from: http://www2.ups.edu/faculty/hanson/labtechniques/refractometry/intro.htm

[8] Moh. Yasin, Sulaiman W. Harun, Hamzah Arof: *Fiber Optic Sensors*. InTech, Fabruary 22, 2012, 530 pages.

[9] Feng De-Jun, Liu Guan-Xiu, Liu Xi-Lu, Jiang Ming-Shun, Sui Qing-Mei: *Refractive index sensor based on plastic optical fiber with tapered structure*. Shandong University, Jinan 250100, China, February 18, 2014.

[10] Ye Tian, Wenhui Wang, Nan Wu, Xiaotian Zou, Xingwei Wang: *Tapered Optical Fiber Sensor for Label-Free Detection of Biomolecules*. University of Massachusetts Lowell, One University Ave., Lowell, MA 01854, USA, March 28, 2011. Available from: http://www.mdpi.com/1424-8220/11/4/3780/htm

[11] K. S. Lim, S. W. Harun, H. Arof, H. Ahmad: *Fabrication and Applications of Microfiber*. University of Malaya, Kuala Lumpur, Malaysia, February, 2012.

[12] S. W. Harun, K. S. Lim, C. K. Tio, K. Dimyati, H. Ahmad: *Theoretical analysis and fabrication of tapered fiber*. Malaysia, December 16, 2011. Available from: http://repository.um.edu.my/35385/1/16.pdf

[13] Feng De-Jun, Zhang Mao-Sen, Guanxiu Liu, Liu Xi-Lu, Jia Dong-Fang: *D-shaped Plastic Optical Fiber Sensor for Testing Refractive Index*. IEEE SENSORS JOURNAL, May 2014. Available from: http://ieeexplore.ieee.org/stamp/stamp.jsp?arnumber=6717983

[14] Hummad Habib Qazi, Abu Bakar Mohammad, Harith Ahmad, Mohd Zamani Zulkifli: *D-shaped Polarization Maintaining Fiber Sensor for Strain Temperature Monitoring*. Malaysia, September 15, 2016. Available from: http://www.mdpi.com/1424-8220/16/9/1505/pdf

[15] LEONI FIBER OPTICS, INC. *Standard POF*. Spec Sheet, 2005. Available from: http://www.leoni-fiber-optics.com/fileadmin/bu/fo/produkte/pdf/fasern/pof/pof-standard.pdf

[16] OCEAN OPTICS, INC. *Halogen Light Source with Attenuator and TTL-Shutter*. Installation and Operation Manual, April 2015. Available from: https://oceanoptics.com/wp-content/uploads/hl2000fhsa1.pdf

[17] OCEAN OPTICS, INC. *Light Sources.* Available from: https://oceanoptics.com/wp-content/uploads/Ocean_Optics_Light_Sources.pdf

[18] THORLABS, INC. *Optical Power and Energy Meter PM100D.* Operation Manual, April 2011. Available from: https://www.thorlabs.com/drawings/9506fcbc1ea7e7fa-EB95FB08-5056-2306-D9AD91C652BEB422/PM100D-Manual.pdf

[19] THORLABS, INC. *Compact Photodiode Power Head with Silicon Detector S121C.* Spec Sheet, February 2016. Available from: https://www.thorlabs.com/drawings/9506fcbc1ea7e7fa-EB95FB08-5056-2306-D9AD91C652BEB422/S121C-SpecSheet.pdf

[20] THORLABS, INC. *Bare Fiber Optic Terminators BFT1 with B10510A Multimode SMA905 Connectors.* Available from: https://www.thorlabs.com/newgrouppage9.cfm?objectgroup_ID=8543

[21] THORLABS, INC. *FN96A.* Guide to Connectorization and Polishing Optical Fibers, December 15, 2015. Available from: https://www.thorlabs.com/drawings/9506fcbc1ea7e7fa-EB95FB08-5056-2306-D9AD91C652BEB422/FN96A-Manual.pdf

[22] EUROLABPEAN FEDERATION OF NATIONAL ASSOCIATIONS OF MEASUREMENT, TESTING AND ANALYTICAL LABORATORIES. *Guide to the Evaluation of Measurement Uncertainty for Quantitative Test Results.* Technical Report, August 2006. Available from: http://www.eurolab.org/documents/EL_11_01_06_387%20Technical%20report%20-%20Guide%20Measurement%20uncertainty.pdf

[23] *Measurement Uncertainty.* MARLAP Manual Volume III: Chapter 19, July 2004. Available from: https://www.epa.gov/sites/production/files/2015-05/documents/402-b-04-001c-19-final.pdf

[24] *Nejistoty měření.* Dodatek k monografii Haasz V., Sedláček M.: *Elektrická měření: přístroje a metody.* ČVUT, Praha, 2003. Available from: http://measure.feld.cvut.cz/cs/system/files/files/cs/vyuka/predmety/a1b38ema/pdfs_nejistoty_dodatek_monografie.pdf

[25] *Expanded uncertainty and coverage factor.* National Institute of Standards and Technology. Available from: http://physics.nist.gov/cuu/Uncertainty/coverage.html

[26] Filipa Sequeira, Daniel Duarte, Lucia Birlo, Alisa Rudnitskaya, Maria Pesavento, Luigi Zeni, Nunzio Cennamo: *Refractive Index Sensing with D-Shaped Plastic Optical Fibers for Chemical and Biochemical Applications*. Basel, Switzerland, December 13, 2016. Available from: https://www.ncbi.nlm.nih.gov/pmc/articles/PMC5191099/pdf/sensors-16-02119.pdf

[27] George Y. Chen, Ming Ding, Trevor. P. Newson, Gilberto Brambilla: *A Review of Microfiber and Nanofiber Based Optical Sensors*. Optoelectronics Research Centre, University of Southampton, Southampton, United Kingdom, December 2, 2013. Available from: https://benthamopen.com/contents/pdf/TOOPTSJ/TOOPTSJ-7-32.pdf

Appendix – The results of the measurement uncertainties evaluation

	↓ n, [-]	i →	1	2	3	4	5	6	7	8	9	10	$u_{A(P)}$, [μW]	$u_{B(P)}$, [μW]	$u_{C(P)}/u_C$, [μW/dBm]	$P \pm {}_{\Delta}P$, **[dBm]**
unbent structure	1,45027	***P*, [dBm]**	-11,38	-11,41	-11,35	-11,40	-11,36	-11,33	-11,41	-11,33	-11,42	-11,37			0,15	**-11,4 ± 0,2**
		***P*, [μW]**	72,78	72,28	73,28	72,44	73,11	73,62	72,28	73,62	72,11	72,95	0,1770	1,2849	2,59	
	1,45721	***P*, [dBm]**	-11,80	-11,76	-11,77	-11,82	-11,83	-11,79	-11,80	-11,66	-11,79	-11,81			0,16	**-11,8 ± 0,2**
		***P*, [μW]**	66,07	66,68	66,53	65,77	65,61	66,22	66,07	68,23	66,22	65,92	0,2341	1,1720	2,39	
	1,46336	***P*, [dBm]**	-12,35	-12,28	-12,25	-12,30	-12,33	-12,27	-12,30	-12,34	-12,37	-12,42			0,16	**-12,3 ± 0,2**
		***P*, [μW]**	58,21	59,16	59,57	58,88	58,48	59,29	58,88	58,34	57,94	57,28	0,2186	1,0381	2,12	
	1,47126	***P*, [dBm]**	-13,15	-13,08	-13,05	-13,11	-12,99	-13,04	-13,07	-13,10	-13,02	-13,09			0,16	**-13,1 ± 0,2**
		***P*, [μW]**	48,42	49,20	49,55	48,87	50,23	49,66	49,32	48,98	49,89	49,09	0,1672	0,8773	1,79	
U-shaped structure R = 6 mm	1,45027	***P*, [dBm]**	-12,37	-12,43	-12,43	-12,52	-12,47	-12,52	-12,38	-12,43	-12,40	-12,38			0,16	**-12,4 ± 0,2**
		***P*, [μW]**	57,94	57,15	57,15	56,10	56,62	55,98	57,81	57,15	57,54	57,81	0,2209	1,0126	2,07	
	1,45721	***P*, [dBm]**	-13,44	-13,39	-13,38	-13,41	-13,34	-13,39	-13,36	-13,42	-13,40	-13,35			0,16	**-13,4 ± 0,2**
		***P*, [μW]**	45,29	45,81	45,92	45,60	46,34	45,81	46,13	45,50	45,71	46,24	0,1051	0,8171	1,65	
	1,46336	***P*, [dBm]**	-14,84	-14,80	-14,73	-14,79	-14,77	-14,80	-14,81	-14,78	-14,72	-14,78			0,16	**-14,8 ± 0,2**
		***P*, [μW]**	32,81	33,11	33,65	33,19	33,34	33,11	33,04	33,27	33,73	33,27	0,0869	0,5990	1,21	
	1,47126	***P*, [dBm]**	-18,47	-18,52	-18,58	-18,65	-18,60	-18,49	-18,61	-18,58	-18,56	-18,53			0,17	**-18,6 ± 0,2**
		***P*, [μW]**	14,22	14,06	13,87	13,65	13,80	14,16	13,77	13,87	13,93	14,03	0,0569	0,2645	0,54	
U-shaped structure R = 4 mm	1,45027	***P*, [dBm]**	-14,28	-14,31	-14,25	-14,29	-14,31	-14,32	-14,30	-14,28	-14,27	-14,28			0,16	**-14,3 ± 0,2**
		***P*, [μW]**	37,33	37,07	37,58	37,24	37,07	36,98	37,15	37,33	37,41	37,33	0,0579	0,6683	1,34	
	1,45721	***P*, [dBm]**	-14,90	-14,88	-14,93	-14,91	-14,88	-14,87	-14,85	-14,88	-14,90	-14,87			0,16	**-14,9 ± 0,2**
		***P*, [μW]**	32,36	32,51	32,14	32,28	32,51	32,58	32,73	32,51	32,36	32,58	0,0542	0,5853	1,18	
	1,46336	***P*, [dBm]**	-16,29	-16,30	-16,26	-16,27	-16,31	-16,28	-16,32	-16,29	-16,26	-16,27			0,16	**-16,3 ± 0,2**
		***P*, [μW]**	23,50	23,44	23,66	23,60	23,39	23,55	23,33	23,50	23,66	23,60	0,0354	0,4305	0,86	
	1,47126	***P*, [dBm]**	-20,18	-20,23	-20,21	-20,24	-20,20	-20,25	-20,22	-20,19	-20,21	-20,18			0,17	**-20,2 ± 0,2**
		***P*, [μW]**	9,59	9,48	9,53	9,46	9,55	9,44	9,51	9,57	9,53	9,59	0,0167	0,1882	0,38	